

Magnonic Weyl semimetal in pyrochlore ferromagnets

Ying Su^{1,2}, X. S. Wang^{1,2}, and X. R. Wang^{1,2*}

¹*Physics Department, The Hong Kong University of Science and Technology, Clear Water Bay, Kowloon, Hong Kong and*

²*HKUST Shenzhen Research Institute, Shenzhen 518057, China*

(Dated: October 2, 2016)

Topological states of matter have been a subject of intensive studies in recent years because of their exotic properties such as the topologically protected edge and surface states. The initial studies were exclusively for electron systems. It is now known that topological states can also exist for other particles. Indeed, topologically protected edge states have already been found for phonons and photons. In spite of active searching for topological states in many fields, the studies in magnetism are relatively rare although topological states are apparently important and useful in magnonics. Here we show that the pyrochlore ferromagnets with the Dzyaloshinskii-Moriya interaction are intrinsic magnonic Weyl semimetals. Similar to the electronic Weyl semimetals, the magnon bands in a magnonic Weyl semimetal are nontrivially crossing in pairs at special points (called Weyl nodes) in momentum space. The equal energy contour around the Weyl nodes gives rise to the Fermi arcs on sample surfaces due to the topologically protected surface states between each pair of Weyl nodes. Additional Weyl nodes and Fermi arcs can be generated in lower energy magnon bands when an anisotropic exchange interaction is introduced.

PACS numbers:

I. INTRODUCTION

Magnetic materials are highly correlated spin systems that do not respect time-reversal symmetry. Their static states, such as domains, domain walls, and skyrmions, are the energy minimum spatial configurations of magnetization (vector order parameter)¹. The excitations of magnetic materials are spin waves whose quanta are magnons of spin-1 particles. Like electrons, magnons can carry, process and transmit information besides being a control knob of magnetization dynamics²⁻⁴. In fact, magnonics⁵⁻¹² is a very active research field because of low energy consumption of magnonic devices and possible long spin coherence length¹³⁻¹⁵. One important issue in magnonics is the efficient transportation of magnons. Magnon (spin wave) flux normally decays fast during its propagation because it is difficult to confine magnons in the space. Finding materials or structures that can confine the motion of magnons in a restricted region under topological protection should open doors to new functional devices. Thus, the realization of topological states of matter in magnetic systems should be highly desirable¹⁶⁻¹⁸.

In this work, we show that the pyrochlore ferromagnet $\text{Lu}_2\text{V}_2\text{O}_7$, which was recently shown to exhibit magnon Hall effect¹⁹, is an intrinsic magnonic Weyl semimetal (MWS). Two adjacent magnon bands in a MWS nontrivially cross each other at some special points called Weyl nodes (WNs) in momentum space. The WNs are monopoles of Berry curvature and are characterized by integer topological charges. Because the net topological charges in the entire Brillouin zone (BZ) must be zero, the WNs must appear in pairs with opposite topological charges²⁰. Like the electronic Weyl semimetal, the MWS has topologically protected chiral surface states between each pair of WNs on the sample surfaces²¹⁻²³. The equal

energy contour of these surface states form arcs (called Fermi arc), and the number of Fermi arcs between two paired WN equals to the number of topological charges carried by one of them. Moreover, additional WN and topologically protected surface states can appear in lower energy magnon bands when anisotropic exchange interaction, possibly induced by either doping or strain along the [111] direction, is introduced.

II. RESULTS

A. The effective spin model of $\text{Lu}_2\text{V}_2\text{O}_7$

$\text{Lu}_2\text{V}_2\text{O}_7$ is an intrinsic ferromagnetic Mott-insulator in which each vanadium ion V^{4+} carries spin $S = 1/2$ ^{19,24}. The magnetic properties of the material come purely from the vanadium ions that form a pyrochlore lattice consisting of four interpenetrating face-centered cubic (FCC) lattices with corner-sharing tetrahedrons, as shown in Fig. 1a. The primitive vectors are $\mathbf{a}_1 = (1, 1, 0)/2$, $\mathbf{a}_2 = (1, 0, 1)/2$, and $\mathbf{a}_3 = (0, 1, 1)/2$, where the FCC lattice constant is set to unit. Three of the four FCC lattices are shifted by $\mathbf{a}_1/2$, $\mathbf{a}_2/2$, and $\mathbf{a}_3/2$, respectively. In each unit cell, there are four V^{4+} ions as shown in Fig. 1b. Under an external magnetic field, the magnetic properties of the material is well described by a simple Heisenberg Hamiltonian with the Dzyaloshinskii-Moriya interaction (DMI)¹⁹. The effective spin Hamiltonian reads

$$H = - \sum_{\langle ij \rangle} J_{ij} \mathbf{S}_i \cdot \mathbf{S}_j + \sum_{\langle ij \rangle} \mathbf{D}_{ij} \cdot (\mathbf{S}_i \times \mathbf{S}_j) - g\mu_B \sum_i \mathbf{h} \cdot \mathbf{S}_i, \quad (1)$$

where $\langle ij \rangle$ denotes the nearest neighbor (NN) sites and \mathbf{S}_i is the spin of the V^{4+} ion at site i . \mathbf{h} is the external

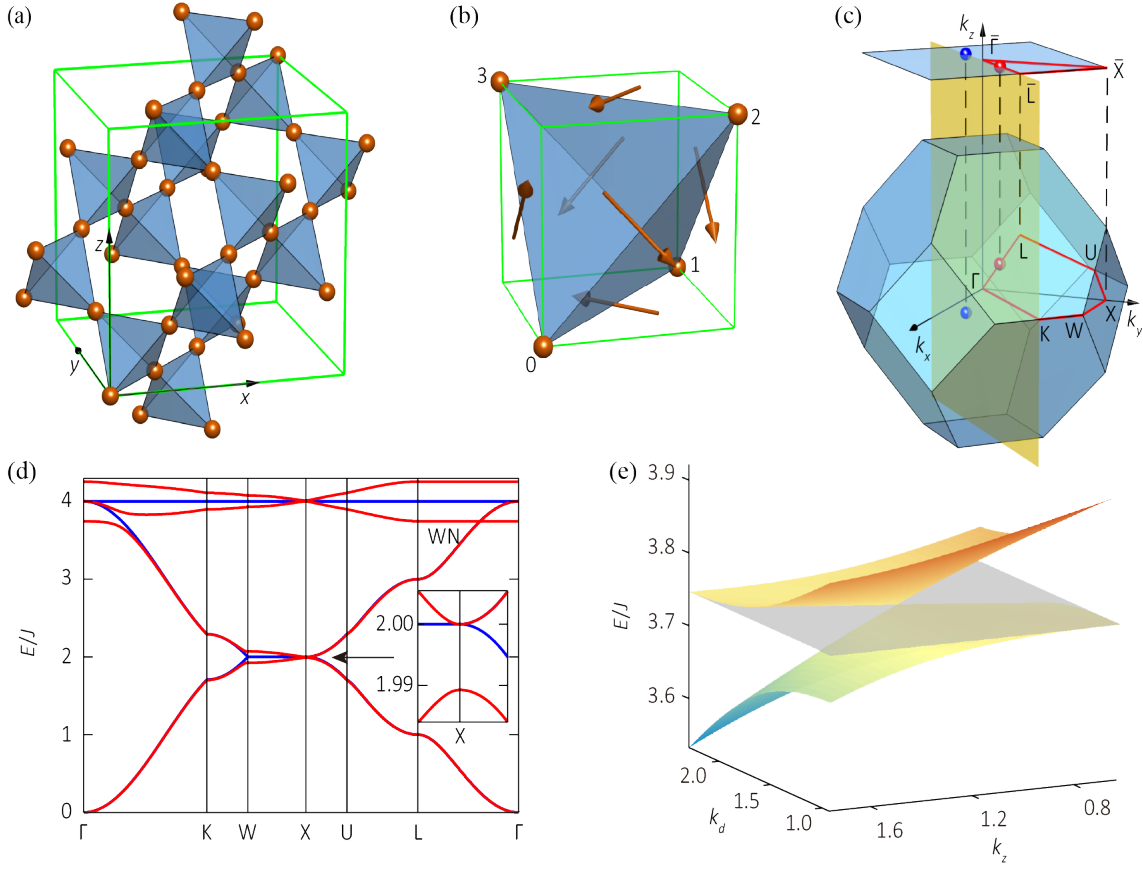


FIG. 1: (a) The pyrochlore structure of four interpenetrating face-centered cubic lattices with corner-sharing tetrahedrons. The orange dots denote the V^{4+} ions. (b) The DMI vector configuration of a tetrahedron lying in a corner-sharing cubic. The arrows represent the DMI vectors \mathbf{D}_{ij} perpendicular to the bonds of the tetrahedron and parallel to the surfaces of the cubic. (c) The first bulk Brillouin zone (BZ) and the first (001) surface BZ of the pyrochlore lattice. The projection of the high symmetry points of the bulk BZ onto the surface BZ are denoted by the barred symbols. The red and blue dots schematically represent the pair of WNs with opposite topological charges between E_2 and E_3 bands. (d) The magnon energy spectrum along the high symmetry path shown in (c) with DMI (red curves) and without DMI (blue curves). (e) The magnon dispersion around the WN shown in (d) in the k_z - k_d plane which is represented by the yellow plane in (c).

magnetic field applied along the [111] direction in this study. The first term describes the NN exchange interaction with strengths J_{ij} . The second term represents the DMI with the DMI vectors \mathbf{D}_{ij} . The last term is the Zeeman interaction.

As it was explained in ref. 19, the material is a collinear ferromagnet in spite of the DMI because the summation of six DMI vectors adjacent to each lattice site is zero. Under the Holstein-Primakoff transformation and by using the Bloch theorem, the Hamiltonian (1) is block diagonalized in momentum space as $H = \sum_{\mathbf{k}} b_{\mathbf{k}}^\dagger \mathcal{H}(\mathbf{k}) b_{\mathbf{k}} + E_0$, where $b_{\mathbf{k}}^\dagger = (b_{\mathbf{k},0}^\dagger, b_{\mathbf{k},1}^\dagger, b_{\mathbf{k},2}^\dagger, b_{\mathbf{k},3}^\dagger)$ and $b_{\mathbf{k}}$ are the creation and annihilation operators of magnons (see Methods). The four components correspond to the four different FCC sublattices. $E_0 = -Ng\mu_B|\mathbf{h}|/2 - \sum_i \sum_{j \in \langle ij \rangle} J_{ij}/8$ is the energy of zero magnon state (vacuum), where N is the total number of lattice sites and $j \in \langle ij \rangle$ denotes j as the NN site of i (see Methods). One can set E_0 to zero by choosing a proper energy reference. For a given

\mathbf{k} , $\mathcal{H}(\mathbf{k})$ is a 4×4 matrix

$$\mathcal{H}(\mathbf{k}) = \begin{pmatrix} 3J & JA_1(\mathbf{k}) & JA_2(\mathbf{k}) & JA_3(\mathbf{k}) \\ JA_1(\mathbf{k}) & 3J & J_- A_{12}(\mathbf{k}) & J_+ A_{13}(\mathbf{k}) \\ JA_2(\mathbf{k}) & J_+ A_{12}(\mathbf{k}) & 3J & J_- A_{23}(\mathbf{k}) \\ JA_3(\mathbf{k}) & J_- A_{13}(\mathbf{k}) & J_+ A_{23}(\mathbf{k}) & 3J \end{pmatrix}, \quad (2)$$

where $A_\alpha(\mathbf{k}) = -\cos(\mathbf{a}_\alpha \cdot \mathbf{k}/2)$, $A_{\alpha\beta}(\mathbf{k}) = -\cos[(\mathbf{a}_\alpha - \mathbf{a}_\beta) \cdot \mathbf{k}/2]$, and $J_{ij} = J$ for isotropic exchange interaction. The strength of the DMI is a constant $D = |\mathbf{D}_{ij}|$. Because only the components of \mathbf{D}_{ij} parallel to the external magnetic field contribute to Hamiltonian (1) (see Methods), $J_\pm = J \pm i\sqrt{2}D/\sqrt{3}$ for \mathbf{h} along the [111] direction^{16,19}. The magnitude of magnetic field is set as $|\mathbf{h}| = 0^+$ for simplicity (and without loss of generality) since the Zeeman interaction only shifts the magnon dispersion relation and does not affect the topological properties. In the absence of DMI $D = 0$, the magnon spectrum contains two degenerate flat bands $E_i(\mathbf{k}) = 4J$ ($i = 1, 2$) and two dispersive

bands $E_i(\mathbf{k}) = 2J \pm J\sqrt{1+F(\mathbf{k})}$ ($i = 3, 4$), where $F(\mathbf{k}) = \cos(k_x/2)\cos(k_y/2) + \cos(k_x/2)\cos(k_z/2) + \cos(k_y/2)\cos(k_z/2)$. The magnon dispersion relation along the high symmetry path Γ -K-W-X-U-L- Γ (see Fig. 1c) is shown in Fig. 1d for $D = 0$ (blue curves) and for the experimental value $D = 0.18J^{25}$ (red curves). In comparison with the case of $D = 0$, the flat bands become dispersive and band gaps are opened.

B. Identification of Weyl nodes and Fermi arcs

Interestingly, a pair of WNs appears on the high symmetry line L- Γ -L as shown in Figs 1c and 1d. Two magnon bands of E_2 and E_3 linearly cross each other, giving rise to a MWS behavior. Along the L- Γ -L line, where $\mathbf{k} = k_1(1, 1, 1)$, two magnon bands are flat with $E_i(\mathbf{k}) = 4J \pm \sqrt{2}D$ ($i = 1, 2$), and the other two bands are dispersive with $E_i(\mathbf{k}) = 2J \pm J\sqrt{2.5 + 1.5\cos k_1}$ ($i = 3, 4$). For $D = 0$, E_3 touches E_1 and E_2 at the Γ point. For modest $D > 0$, E_1 and E_2 are split into two nondegenerate flat bands, and E_2 and E_3 cross at a pair of WNs at

$$k_1 = \pm \cos^{-1} \left[\frac{2(2J - \sqrt{2}D)^2 - 5J^2}{3J^2} \right]. \quad (3)$$

$k_1 = \pm 1.198$ for $D = 0.18J$. Moreover, the flatness of E_2 along the L- Γ -L line means the magnon group velocity near the WNs vanishes along the [111] direction. According to a recent classification²⁶, this corresponds to the transition state from type-I to type-II Weyl semimetals with vanishing group velocity only in one direction. To visualize the magnon dispersion with vanishing group velocity along the [111] direction, we plot the magnon bands of E_2 and E_3 near one WN in a vertical plane (represented by the yellow plane in Fig. 1c) parallel to both k_z direction and the diagonal k_x - k_y direction (termed as k_d). Obviously, the L- Γ -L line lies in the k_z - k_d plane, and E_2 band and E_3 band linearly cross each other at the WN of $\mathbf{k} = 1.198(1, 1, 1)$ as shown in Fig. 1e.

Similar to the electronic Weyl semimetal, one fingerprint of the MWS is the Fermi arcs on the sample surfaces. In order to illustrate this feature, we consider a slab whose surfaces are perpendicular to the [001] direction. The first BZ of the (001) surface is shown in Fig. 1c, where the projection of the high symmetry points of the first bulk BZ onto the first surface BZ are denoted by the barred symbols. The pair of WNs are schematically represented by the red and blue dots (indicating they carry opposite topological charges) in Fig. 1c. The density plot of magnon spectral function on the top surface along the high symmetry path of $\bar{\Gamma}$ - \bar{X} - \bar{L} - $\bar{\Gamma}$ is shown in Fig. 2a where one WN can be identified. The topologically protected surface states with high density on the top surface are represented by red color. On the path of \bar{L} - $\bar{\Gamma}$ - \bar{L} where both of the two WNs lies

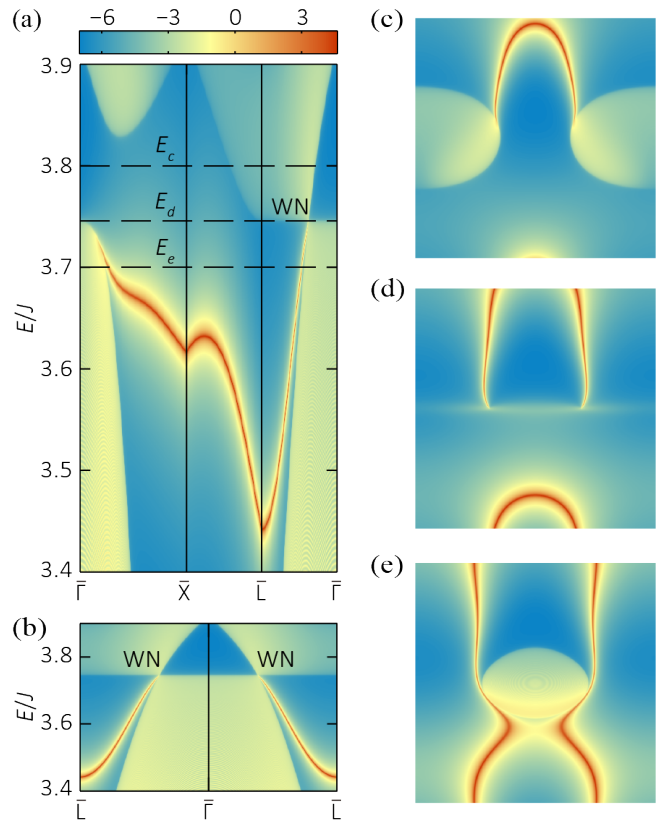


FIG. 2: (a) The density plot of magnon spectral function on the top (001) surface along the $\bar{\Gamma}$ - \bar{X} - \bar{L} - $\bar{\Gamma}$ path. (b) The density plot of magnon spectral function on the top (001) surface along the \bar{L} - $\bar{\Gamma}$ - \bar{L} path. (c)-(e) The density plot of magnon spectral function on the top (001) surface in the first BZ for fixed energies of E_c , E_d , and E_e denoted in (a).

in, the density plot of magnon spectral function on the top surface is shown in Fig. 2b. Apparently, the pair of WNs are connected by surface states. For fixed energies of E_c , E_d , and E_e around the WNs (see Fig. 2a), the corresponding density plot of magnon spectral function on the top surface in the first BZ are shown in Figs 2c-2e, respectively. The Fermi arc formed by topologically protected surface states on the top surface is clearly displayed. For $E_d = 4J - \sqrt{2}D = 3.745J$ through the WNs, the Fermi arc is terminated at the two WNs as shown in Fig. 2d.

C. Anisotropic exchange interaction

We have shown that the pyrochlore ferromagnet $\text{Lu}_2\text{V}_2\text{O}_7$ is an intrinsic MWS. We would like to show now that more pairs of WNs and topologically protected surface states can come from the lower energy magnon bands of E_3 and E_4 in the presence of anisotropic exchange interaction. The pyrochlore lattice can be viewed as an alternative stack of kagome and triangular lattices

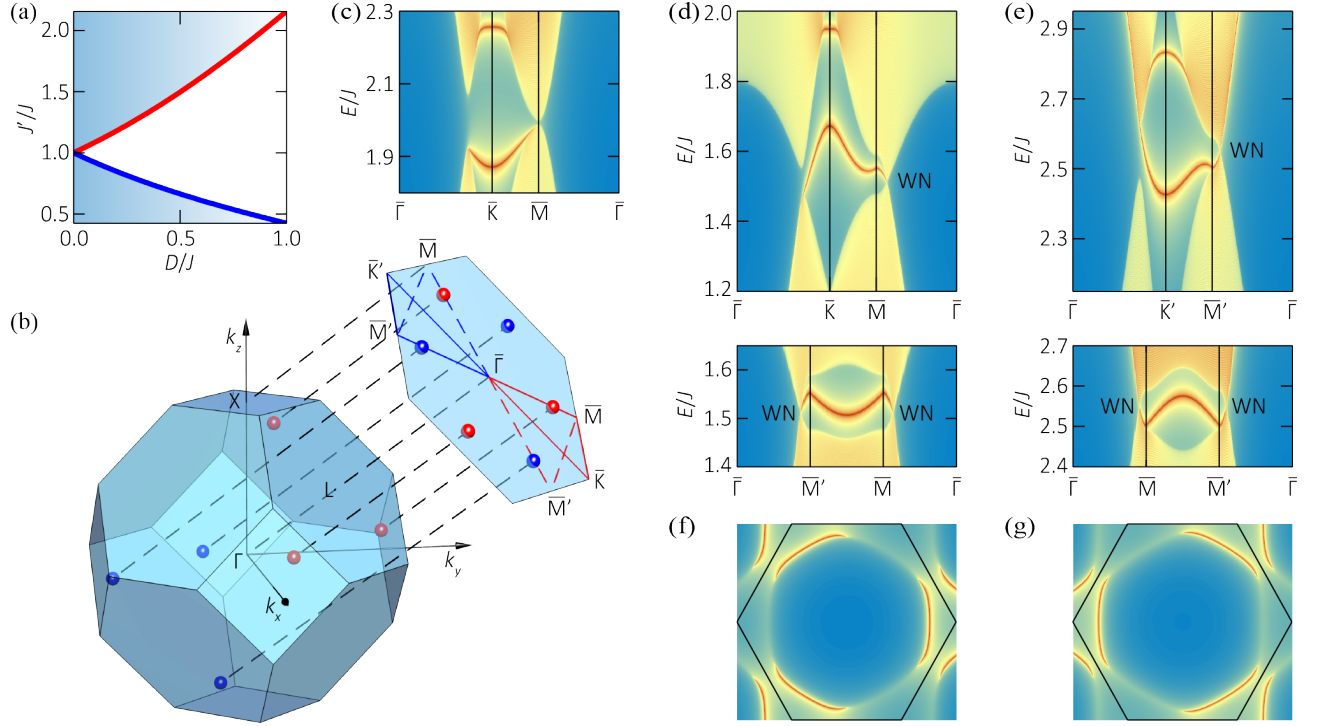


FIG. 3: (a) The phase diagram of the MWS, due to E_3 and E_4 bands, in the D - J' plane. The MWS, together with WNs and Fermi arcs, exists in the shadowed regions. The white region between the two critical interlayer exchange interactions $J'_\pm(D)$ denoted by red and blue curves is the normal magnonic insulator without topologically protected surface states in the energy gap. (b) The first bulk Brillouin zone (BZ) and the first (111) surface BZ of the pyrochlore lattice. The red and blue dots schematically represent the three pairs of WNs with opposite topological charges between the bands of E_3 and E_4 . (c) The density plot of magnon spectral function on the top surface for $J' = J$ along the path of $\bar{\Gamma}$ - \bar{K} - \bar{M} - $\bar{\Gamma}$. (d) The density plot of magnon spectral function on the top surface for $J' = 0.6J$ along the paths of $\bar{\Gamma}$ - \bar{K} - \bar{M} - $\bar{\Gamma}$ (upper panel) and $\bar{\Gamma}$ - \bar{M}' - \bar{M} - $\bar{\Gamma}$ (lower panel) that are presented by red solid and dash lines in (b). (e) The density plot of magnon spectral function on the top surface for $J' = 1.6J$ along the paths of $\bar{\Gamma}$ - \bar{K}' - \bar{M}' - $\bar{\Gamma}$ (upper panel) and $\bar{\Gamma}$ - \bar{M}' - \bar{M}' - $\bar{\Gamma}$ (lower panel) that are presented by blue solid and dash lines in (b). (f)-(g) The Fermi arcs on the top (111) surface for energies through the WNs for $J' = 0.6J < J'_-$ (f) and $J' = 1.6J > J'_+$ (g). The black hexagon encloses the first BZ.

along the [111] direction. In principle, the interlayer exchange interaction J' differs from the intralayer exchange interaction J . J' can be tuned by either doping¹⁶ or strain²⁷. The effective Hamiltonian with the anisotropic exchange interaction, under the same considerations as before, becomes

$$\mathcal{H}'(\mathbf{k}) = \begin{pmatrix} 3J' & J'A_1(\mathbf{k}) & J'A_2(\mathbf{k}) & J'A_3(\mathbf{k}) \\ J'A_1(\mathbf{k}) & 2J + J' & J_-A_{12}(\mathbf{k}) & J_+A_{13}(\mathbf{k}) \\ J'A_2(\mathbf{k}) & J_+A_{12}(\mathbf{k}) & 2J + J' & J_-A_{23}(\mathbf{k}) \\ J'A_3(\mathbf{k}) & J_-A_{13}(\mathbf{k}) & J_+A_{23}(\mathbf{k}) & 2J + J' \end{pmatrix}. \quad (4)$$

The anisotropic exchange interaction leads to different sublattice on-site potential because the one-site potential on each particular site is the sum of the exchange interaction strengths of all its NNs (see Methods).

For the isotropic exchange interaction, the energy gap minimum between E_3 and E_4 bands is at the X point as shown in Fig. 1d. The anisotropic exchange interaction can close the gap at the X point whenever J' equals to

two critical values

$$J'_\pm = \alpha \pm \sqrt{2\alpha^2 - 2\alpha J}, \quad (5)$$

where $\alpha = \sqrt{J^2 + 2D^2/3}$. The critical J'_\pm as functions of the DMI strength D are plotted as red and blue curves in Fig. 3a. These are the phase boundaries between the normal magnonic insulator (without topologically protected surface states in the gap) and the MWS from E_3 and E_4 bands. The phase diagram of the MWS from E_3 and E_4 bands in the D - J' plane is shown in Fig. 3a. In the shadowed regions of Fig. 3a where $J' > J'_+$ or $J'_- > J' > 0$, E_3 and E_4 bands always cross at three pairs of WNs due to the three-fold rotation symmetry with respect to the L- Γ -L line (see Fig. 3b). For $\text{Lu}_2\text{V}_2\text{O}_7$, $J'_+ = 1.158J$ and $J'_- = 0.863J$. In the limits of $J' \rightarrow \infty$ and 0, all these WNs will merge at the L point. The fact that the trivial region represented by white color shrinks as D decreases means that weak DMI is favorable for the existence of WNs between E_3 and E_4 bands since only weak anisotropy (small difference between the interlayer and intralayer exchange

interactions) is required. These results are applicable to other pyrochlore ferromagnets.

D. Additional Weyl nodes and Fermi arcs

To visualize these additional WNs and topologically protected surface states existing in the MWS phase from E_3 and E_4 bands, the magnon spectral function of a slab with (111) surfaces is calculated. The density plot of magnon spectral function on the top surface for $J' = J$ along the high symmetry path $\bar{\Gamma}\text{-}\bar{K}\text{-}\bar{M}\text{-}\bar{\Gamma}$ (marked by red solid lines in Fig. 3b) is shown in Fig. 3c. The energy gap minimum appears at the \bar{M} point to which the X point is projected. As the interlayer exchange interaction decreases to $J' = 0.6J < J'_-$, three pairs of WNs are created from the linear crossing of E_3 and E_4 bands. The density plot of magnon spectral function on the top surface along various paths is shown in Fig. 3d. Along the path of $\bar{\Gamma}\text{-}\bar{K}\text{-}\bar{M}\text{-}\bar{\Gamma}$, a WN is identified on the $\bar{M}\text{-}\bar{\Gamma}$ segment. The topologically protected surface states is clearly visible within the energy gap with one end terminated at the WN. Along the path of $\bar{\Gamma}\text{-}\bar{M}\text{-}\bar{M}\text{-}\bar{\Gamma}$ (represented by red dash lines in Fig. 3b), a pair of WNs is connected by the surface states. Similar results for $J' = 1.6J > J'_+$ are shown in Fig. 3e along the $\bar{\Gamma}\text{-}\bar{K}'\text{-}\bar{M}'\text{-}\bar{\Gamma}$ and $\bar{\Gamma}\text{-}\bar{M}\text{-}\bar{M}'\text{-}\bar{\Gamma}$ paths (marked by blue solid and dash lines, respectively, in Fig. 3b). In order to detect the Fermi arc feature, we fix the energy through the WNs for the two different interlayer exchange interaction strengths. The density plot of magnon spectral function on the top surface in the two-dimensional momentum space is shown in Figs 3f and 3g where the black hexagon encloses the first surface BZ. Apparently, the topologically protected surface states form three Fermi arcs of the three pairs of WNs.

The pair of WNs from E_2 and E_3 bands on the L- Γ -L line can remain for the anisotropic exchange interaction. Since the magnon dispersions on the L- Γ -L line with $\mathbf{k} = k_1(1, 1, 1)$ are $E_2(\mathbf{k}) = 3J + J' - \sqrt{2}D$ and $E_3(\mathbf{k}) = 2J' + J'\sqrt{2.5 + 1.5 \cos k_1}$ in the present case, E_2 and E_3 bands cross at a pair of WNs at

$$k_1 = \pm \cos^{-1} \left[\frac{2(3J - J' - \sqrt{2}D)^2 - 5J'^2}{3J'^2} \right], \quad (6)$$

as long as $J - \sqrt{2}D/3 < J' < 3J/2 - D/\sqrt{2}$. Because the E_2 band is flat along the L- Γ -L line, the magnon group velocity around the pair of WNs vanishes along the [111] direction.

III. DISCUSSION

The pyrochlore ferromagnet $\text{Lu}_2\text{V}_2\text{O}_7$ is an intrinsic topological material (called MWS) in the sense that two

adjacent magnon bulk bands of E_2 and E_3 linearly cross each other at a special pair of points (called WNs) on the L- Γ -L line in momentum space. The distance between the paired WNs is determined by the strength of DMI. Similar to its electronic counterpart, the MWS has topologically protected chiral surface states whose equal energy contour yields the Fermi arc that connects the pair of WNs on the sample surfaces. By introducing different interlayer and intralayer exchange interaction strengths through either doping or strain along the [111] direction, three additional pairs of WNs can be generated from the lower energy magnon bands of E_3 and E_4 . On the surfaces of a slab perpendicular to the [111] direction, the three pairs of WNs are connected by three Fermi arcs in two-dimensional momentum space. Furthermore, the pair of WNs between E_2 and E_3 bands can remain on the L- Γ -L line whose distance is determined by both the DMI and interlayer exchange interaction. These results are applicable to other collinear pyrochlore ferromagnets with anisotropic exchange interaction.

The MWS featured by WNs and Fermi arcs can be detected by inelastic neutron scattering which has been used to probe the magnon bands of a topological magnon insulator¹⁷. The topologically protected magnon surface states can also be probed by the spin-polarized scanning tunneling microscopy through the second-order derivative of tunneling current that contains the information of electron-magnon scattering²⁸.

IV. METHODS

A. Holstein-Primakoff transformation

In this transformation²⁹, the spin-1/2 operators are mapped to the magnon creation and annihilation operators as

$$S_i^+ = \sqrt{1 - n_i} b_i, \quad S_i^- = b_i^\dagger \sqrt{1 - n_i}, \quad n_i = b_i^\dagger b_i, \quad (7)$$

where the ladder operators $S_i^\pm = S_i^l \pm iS_i^m$ are defined in the orthonormal coordinate (l, m, n) with n axis parallel to the external magnetic field. For the DMI, the local spin $\mathbf{S}_i = \mathbf{S} + \delta\mathbf{S}_i$ where $\mathbf{S} = (0, 0, 1/2)$ and $\delta\mathbf{S}_i = (S_i^l, S_i^m, 0)$ in the linear approximation. Thus, the Hamiltonian of DMI is

$$\begin{aligned} H_{\text{DMI}} &= \sum_{\langle ij \rangle} \mathbf{D}_{ij} \cdot (\mathbf{S} \times \delta\mathbf{S}_j + \delta\mathbf{S}_i \times \mathbf{S} + \delta\mathbf{S}_i \times \delta\mathbf{S}_j) \\ &= \sum_{\langle ij \rangle} \mathbf{D}_{ij} \cdot (0, 0, S_i^l S_j^m - S_i^m S_j^l) \\ &= \sum_{\langle ij \rangle} \frac{iD_{ij}^n}{2} (S_i^+ S_j^- - S_i^- S_j^+), \end{aligned} \quad (8)$$

where $D_{ij}^n = \mathbf{D}_{ij} \cdot \hat{n}$ and $\sum_{\langle ij \rangle} \mathbf{D}_{ij} \cdot (\mathbf{S} \times \delta\mathbf{S}_j + \delta\mathbf{S}_i \times \mathbf{S}) = 0$. Namely, the \mathbf{D}_{ij} with vanishing n component does

not contribute to the Hamiltonian. Substitute these into the effective spin Hamiltonian (1), we get a tight-binding Hamiltonian of magnons as

$$H = -\frac{1}{2} \sum_{\langle ij \rangle} \left[(J_{ij} + iD_{ij}^n) b_i^\dagger b_j + \text{H.c.} \right] + E_0, \quad (9)$$

$$+ \sum_i \left(\sum_{j \in \langle ij \rangle} \frac{J_{ij}}{2} + g\mu_B |\mathbf{h}| \right) b_i^\dagger b_i.$$

Here $j \in \langle ij \rangle$ denotes j as the NN site of i , and $E_0 = -Ng\mu_B |\mathbf{h}|/2 - \sum_i \sum_{j \in \langle ij \rangle} J_{ij}/8$ can be set to zero by choosing a proper energy reference, where N is the total number of lattice sites. Moreover, the on-site potential of each lattice site is determined by the sum of all adjacent NN exchange interaction strengths such that the anisotropic exchange interaction can generate different sublattice on-site potential as shown in equation (4).

According to the Bloch theorem, the Hamiltonian (4) is block diagonalized in the basis of Bloch states

$$|\mathbf{k}, \alpha\rangle = \frac{1}{\sqrt{N/4}} \sum_i e^{i\mathbf{k}\cdot\mathbf{r}_i} |i, \alpha\rangle, \quad (10)$$

where $\alpha = 0, 1, 2, 3$ denote four different sublattices shown in Fig. 1b and \mathbf{r}_i is the position of the i th unit

cell. Thus, we obtain the Hamiltonian (2) and (4).

B. Surface spectral function.

The spectral function of a specific layer is

$$A_l(\mathbf{k}, E) = -\frac{1}{\pi} \text{Im} [\text{Tr} G_{ll}(E, \mathbf{k})], \quad (11)$$

where l is the layer index and $G_{ll}(E, \mathbf{k}) = \langle l | (E + i0^+ - H)^{-1} | l \rangle$. For the top surface with $l = 1$, $G_{11}(E, \mathbf{k})$ is obtained by the recursive Green's function method^{30,31}.

Note added. Upon completion of this work, we became aware of ref. 32, in which part of the results were obtained.

V. ACKNOWLEDGMENTS

This work is supported by the NSF of China Grant (No. 11374249) and Hong Kong RGC Grants (No. 163011151 and No. 605413).

-
- * corresponding author: phxwan@ust.hk
- ¹ Stöhr, J. & Siegmann, H. C. *Magnetism: From Fundamentals to Nanoscale Dynamics* (Springer, 2006).
 - ² Yan, P., Wang, X. S. & Wang, X. R. All-magnonic spin-transfer torque and domain wall propagation. *Phys. Rev. Lett.* **107**, 177207 (2011).
 - ³ Wang, X. S., Yan, P., Shen, Y. H., Bauer, G. E. W. & Wang, X. R. Domain wall propagation through spin wave emission. *Phys. Rev. Lett.* **109**, 167209 (2012).
 - ⁴ Hu, B. & Wang, X. R. Instability of walker propagating domain wall in magnetic nanowires. *Phys. Rev. Lett.* **111**, 027205 (2013).
 - ⁵ Kruglyak, V. V. & Hicken, R. J. Magnonics: experiment to prove the concept. *J. Magn. Magn. Mater.* **306**, 191-194 (2006).
 - ⁶ Neusser, S. & Grundler, D. Magnonics: spin waves on the nanoscale. *Adv. Mater.* **21**, 2927-2932 (2009).
 - ⁷ Khitun, A., Bao, M. & Wang, K. L. Magnonic logic circuits. *J. Phys. D* **43**, 264005 (2010).
 - ⁸ Lenk, B., Ulrichs, H., Garbs, F. & Mnzenberg, M. The building blocks of magnonics. *Phys. Rep.* **507**, 107-136 (2011).
 - ⁹ Kruglyak, V. V., Demokritov, S. O. & Grundler, D. Magnonics. *J. Phys. D: Appl. Phys.* **43**, 26030 (2010).
 - ¹⁰ Demokritov, S. O. & Slavin, A. N. *Magnonics From Fundamentals to Applications* (Topics in Applied Physics Vol. 125, Springer, 2013).
 - ¹¹ Grundler, D. Reconfigurable magnonics heats up. *Nature Phys.* **11**, 438-441 (2015).
 - ¹² Chumak, A. V., Vasyuchka, V. I., Serga, A. A. & Hillebrands, B. Magnon spintronics. *Nature Phys.* **11**, 453-461 (2015).
 - ¹³ Kajiwara, Y. *et al.* Transmission of electrical signals by spin-wave interconversion in a magnetic insulator. *Nature* **464**, 262-266 (2010).
 - ¹⁴ Cornelissen, L. J., Liu, J., Duine, R. A., Youssef, J. B. & van Wees, B. J. Long-distance transport of magnon spin information in a magnetic insulator at room temperature. *Nature Phys.* **11**, 1022-1026 (2015).
 - ¹⁵ Giles, B. L., Yang, Z., Jamison, J. & Myers, R. C. Long-range pure magnon spin diffusion observed in a nonlocal spin-Seebeck geometry. *Phys. Rev. B* **92**, 224415 (2015).
 - ¹⁶ Zhang, L., Ren, J., Wang, J. S. & Li, B. Topological magnon insulator in insulating ferromagnet. *Phys. Rev. B* **87**, 144101 (2013).
 - ¹⁷ Chisnell, R. *et al.* Topological magnon bands in a kagome lattice ferromagnet. *Phys. Rev. Lett.* **115**, 147201 (2015).
 - ¹⁸ Li, F. Y. *et al.* Weyl magnon. Preprint at <http://arxiv.org/abs/1602.04288> (2016).
 - ¹⁹ Onose, Y., Ideue, T., Katsura, H., Shiomi, Y., Nagaosa, N. & Tokura, Y. Observation of the magnon Hall effect. *Science* **329**, 297-299 (2010).
 - ²⁰ Nielsen, H. B. & Ninomiya, M. The Adler-Bell-Jackiw anomaly and Weyl fermions in a crystal. *Phys. Lett. B* **130**, 389-396 (1983).
 - ²¹ Wan, X., Turner, A. M., Vishwanath, A. & Savrasov, S. Y. Topological semimetal and Fermi-arc surface states in the electronic structure of pyrochlore iridates. *Phys. Rev. B* **83**, 205101 (2011).
 - ²² Xu, S. Y. *et al.* Discovery of a Weyl fermion semimetal and

- topological Fermi arcs. *Science* **349**, 613617 (2015).
- ²³ Lv, B. Q. *et al.* Experimental discovery of Weyl semimetal TaAs. *Phys. Rev. X* **5**, 031013 (2015).
- ²⁴ Ichikawa, H. *et al.* Orbital ordering in ferromagnetic $\text{Lu}_2\text{V}_2\text{O}_7$. *J. Phys. Soc. Jpn.* **74**, 1020 (2005).
- ²⁵ Mena, M. *et al.* Spin-wave spectrum of the quantum ferromagnet on the pyrochlore Lattice $\text{Lu}_2\text{V}_2\text{O}_7$. *Phys. Rev. Lett.* **113**, 047202 (2014).
- ²⁶ Soluyanov, A. A. *et al.* Type-II Weyl semimetals. *Nature* **527**, 495-498 (2015).
- ²⁷ Guo, H. M. & Franz, M. Three-dimensional topological insulators on the pyrochlore lattice. *Phys. Rev. Lett.* **103**, 206805 (2009).
- ²⁸ Balashov, T., Takacs, A. F., Wulfhekel, W. & Kirschner, J. Magnon excitation with spin-polarized scanning tunneling microscopy. *Phys. Rev. Lett.* **97**, 187201 (2006).
- ²⁹ Holstein, T. & Primakoff, H. Field dependence of the intrinsic domain magnetization of a ferromagnet. *Phys. Rev.* **58**, 1098-1113 (1940).
- ³⁰ Lee, P. A. & Fisher, D. S. Anderson localization in two dimensions. *Phys. Rev. Lett.* **47**, 882 (1981).
- ³¹ Thouless, D. J. & Kirkpatrick, S. Conductivity of the disordered linear chain. *J. Phys. C* **14**, 235-245 (1981).
- ³² Mook, A., Henk, J. & Mertig, I. Tunable magnon Weyl points in ferromagnetic pyrochlores. Preprint at <http://arxiv.org/abs/1606.07612> (2016).